nature communications

Article

https://doi.org/10.1038/s41467-025-58016-w

Multimodal feature fusion machine learning for predicting chronic injury induced by engineered nanomaterials

Received: 22 October 2023

Accepted: 11 March 2025

Published online: 20 March 2025

Check for updates

Yang Huang[1,2,7], Jiayu Cao[3,7], Xuehua Li[1] ✉, Qing Yang[3], Qianqian Xie[4], Xi Liu[4], Xiaoming Cai[3] ✉, Jingwen Chen[1], Huixiao Hong[5] & Ruibin Li[4,6] ✉

Concerns regarding chronic injuries (*e.g.*, fibrosis and carcinogenesis) induced by nanoparticles raised public health concerns and need to be rapidly assessed in hazard identification. Although in silico analysis is commonly used for risk assessment of chemicals, predicting chronic in vivo nanotoxicity remains challenging due to the intricate interactions at multiple interfaces like nano-biofluids and nano-subcellular organelles. Herein, we develop a multimodal feature fusion analysis framework to predict the fibrogenic potential of metal oxide nanoparticles (MeONPs) in female mice. Treating each nano-bio interface as an independent entity, eighty-seven features derived from MeONP-lung interactions are used to develop a machine learning-based predictive framework for lung fibrosis. We identify cell damage and cytokine (IL-1β and TGF-β1) production in macrophages and epithelial cells as key events closely associated with particle size, surface charge, and lysosome interactions. Experimental validations show that the developed in silico model has 85% accuracy. Our findings demonstrate the potential usefulness of this predictive model for risk assessment of nanomaterials and in assisting regulatory decision-making. While the model is developed based on 52 MeONPs, further validation using a larger nanoparticle library is necessary to confirm its broader applicability.

More than 10,000 nanoproducts have been produced and used in various industries worldwide[1]. During the lifecycle of some nanoproducts, nanoparticles may be released to form aerosols and travel in the air[2]. Inhalation is the major exposure route for airborne nanoparticles and can cause respiratory injury in mammals[3,4]. While certain engineered nanomaterials (ENMs) such as ZnO, CuO, Au, and Ag may produce acute lung inflammation via reactive oxygen species (ROS) generation[5,6], inflammasome activation[7–9], or pro-inflammatory cytokine release[5,7,8,10], other ENMs such as carbon nanotubes and metal oxides may induce chronic respiratory toxicity such as lung fibrosis[11–15] and carcinogenesis[16–18], which are permanent and irreversible lung injuries. The chronic adverse outcomes of ENMs have raised substantial product safety concerns and led to strict regulatory requirements for utilizing nanotechnology. For instance, carbon nanotubes have been added to the Substitute It Now (SIN) list due to their carcinogenic potential[19]. While it is important to note that the SIN list itself lacks regulatory status, chemicals listed therein are frequently identified by the European Chemicals Agency for potential use restrictions. Given the rapid growth in the number of ENMs and their potential to form diverse nanoforms with variations in size, shape, surface

[1]Key Laboratory of Industrial Ecology and Environmental Engineering (MOE), School of Environmental Science and Technology, Dalian University of Technology, Dalian 116024, China. [2]School of Chemistry and Materials Science, Ludong University, Yantai 264025, China. [3]School of Public Health, Soochow University, Suzhou, Jiangsu 215123, China. [4]State Key Laboratory of Radiation Medicine and Protection, Soochow University, Suzhou, China. [5]National Center for Toxicological Research, U.S. Food and Drug Administration, Jefferson, AR 72079, USA. [6]Nanotechnology Centre, VSB-Technical University of Ostrava, Ostrava-Poruba 70800, Czech Republic. [7]These authors contributed equally: Yang Huang, Jiayu Cao. ✉e-mail: lixuehua@dlut.edu.cn; xmcai@suda.edu.cn; liruibin@suda.edu.cn

chemistry, crystallinity, and other attributes, a large number of animals would need to be sacrificed to adequately assess the risk of these nanoforms. It was estimated that the in vivo toxicity assessment of the first generation of ENMs in commercial use may take up to 50 years and cost billions of dollars[20]. To address this challenge, in silico predictive models have been developed to reduce experimental costs.

In recent years, there have been several attempts to predict the in vitro toxicity of nanoparticles[10,21–29]. ENM-induced cytotoxicity, including cell death and inflammatory effects, is often caused by a molecular initiating event (MIE) that is highly dependent on the physicochemical properties of ENMs[10,24,25,27]. To establish in silico models, physicochemical properties have been extensively exploited to identify predictive features. For instance, Labouta et al. found that the cytotoxicity of ENMs could be primarily predicted based on their material chemistry, followed by nanoparticle size and concentration, cell type, and cytotoxicity biomerkers[24]. The surface chemistry, lipophilicity, zeta potential, shape, and size of ENMs also impact their uptake and toxicology behaviors[30,31]. In addition, in silico analysis has been widely used to explore the quantitative structure-activity relationships (QSAR) of ENMs in various cell types, such as human lung cells[26,32], RAW 264.7 cells[23,33], human keratinous cells (HaCaT)[34], THP-1 cells[10], HepRG cells[35,36], and *Escherichia coli*[37,38] for hazard ranking. However, there is no reliable model to predict the chronic respiratory toxicity of ENMs in vivo, such as lung fibrosis. The adverse outcome pathway (AOP) leading to lung fibrosis is characterized by complex interactions among toxicants, immune cells, epithelial cells, and fibroblasts[39,40]. These intricate interactions initiate a cascade of key events that play a pivotal role in the development of lung fibrosis. These events include alterations in lung components, heightened secretion of pro-inflammatory mediators, the influx of inflammatory cells, compromised integrity of the alveolar-capillary membrane, activation of Th2 cells, intensified fibroblast proliferation, and increased collagen deposition. The prediction of chronic toxicity is a major challenge in nanotoxicity studies, as it involves multiple sequential nano-bio interactions that cannot be entirely mirrored at one specific nano-bio interface. Taking lung fibrosis as an example, its pathogenic progress involves the interactions of nanoparticles with lung lining fluids (LLF), macrophage, and epithelial cells, as well as subcellular organelles such as the plasma membrane, lysosome, mitochondria, and cytoplasmic components.

Herein, we aimed to establish a predictive framework for pulmonary fibrosis induced by metal oxide nanoparticles (MeONPs). Based on the biological fate of MeONPs in the lungs, we prepared a library of 52 MeONPs and collected the potential predictive features at multiple interfaces between MeONPs and biological contexts such as membranes, lysosomes, mitochondria, and other cytoplasmic components (Fig. 1A). We acquired a total of 87 multimodal features and two fibrogenic indexes, which were then subjected to machine learning modeling. To construct predictive frameworks, we employed eight distinct machine learning algorithms: random forest, locally weighted learning, C4.5 decision tree, *k*-nearest neighbor, support vector machine, Bayesnet, decision table, and logistic regression. We thoroughly evaluated performance of the developed predictive models using overall predictive accuracy (*ACC*), Matthews correlation coefficient (MCC), sensitivity (SE), specificity (SP), area under the receiver operating characteristic curve (AUC), and *F1* score. The random forest (RF) model performed the best and was further experimentally validated by five MeONPs. Our study presents the in silico framework for decoding the *in chemico* and in vitro to in vivo extrapolation of ENM-induced lung fibrosis.

Results

Construction of a multimodal database

A high-quality database is essential for building reliable predictive models and identifying key events involved in the pathogenic process of lung fibrosis[41]. However, there is a lack of such a database to define the behaviors of MeONPs and their biological effects at multiple nano-bio interfaces. Therefore, we constructed a reliable database of 52 MeONPs by characterizing their physicochemical properties, examining their interactions with biological fluids and subcellular organelles, and assessing their fibrogenic effects in mouse lungs by detecting collagen deposition in lung tissues and TGF-β1 release in bronchoalveolar lavage fluid (BALF).

The selection of these 52 MeONPs was driven by the aim to create a dataset that is both diverse and relevant, thereby contributing meaningfully to the development of a predictive framework for MeONP-induced pulmonary fibrosis. Firstly, we endeavored to establish a diverse MeONP library, encompassing various chemical compositions, sizes, surface charges, and shapes. This diversity is pivotal for acquiring a satisfactory dataset size, allowing the construction of a predictive model applicable to a broad spectrum of MeONPs. Secondly, guided by insights from literature reports, we intentionally included some MeONPs with known fibrogenic (such as TiO_2[42], NiO[43], and CuO[44]) and non-fibrogenic (such as CeO_2[45] and Fe_2O_3[46]) characteristics. This deliberate selection ensures that our dataset not only captures diversity but also aligns with the current understanding of nanotoxicity in the field. Lastly, we carefully considered the feasibility of obtaining the desired MeONPs, weighing options such as commercial sources, in-house synthesis, or donations. For detailed information on the sources and characterization data of the 52 MeONPs, please refer to Supplementary Data 1.

Nano-bio interactions occur mainly in the pulmonary alveoli, which consist of LLF, macrophages, and epithelial cells. Initially, inhaled MeONPs may interact with the LLF, altering their surface chemistry and dispersion states and dissolving to release metal ions. We therefore examined the behavior of MeONPs in simulated lung fluid (SLF) (Supplementary Data 1). Then, the MeONPs may interact with lung cells. We specifically chose macrophages (THP-1) and bronchial epithelial cells (BEAS-2B) for incubation with MeONPs. This selection is rooted in the pivotal roles these cells play in the initiation and progression of lung fibrosis[47], where they release signal molecules that foster inflammation and fibroblast proliferation.

To visualize the intracellular path of MeONPs, we randomly selected ten MeONPs, including α-Al_2O_3, TiO_2-1, La_2O_3, MnO_2-1, Co_3O_4-3, InO_2-1, CeO_2-2, and Nd_2O_3, Bi_2O_3, and Fe_2O_3, which were conjugated with fluorescein isothiocyanate (FITC) for fluorescence microscopy imaging. As shown in Fig. 1B and Fig. S1, the labeled MeONPs showed a time-dependent cascaded distribution pattern from the extracellular matrix into the membrane, lysosome, and cytoplasm. At 8–16 h, the MeONPs overlapped nicely with lysosomes (Fig. 1C). Although the cellular imaging results were not directly incorporated into the construction of any predictive models, these outcomes provided crucial insights for defining key nano-bio interfaces, enhancing our understanding of MeONP interactions within cellular environments.

Considering the acidic and enzymatic traits of lysosomes, we also examined the dissolution of MeONPs in phagolysosomal simulated fluid (PSF) (Supplementary Data 1). Based on the distribution features of MeONPs, we examined the impacts of MeONPs on the cell membrane, lysosome, mitochondria activity, energy production, and redox-homeostasis by detecting lactate dehydrogenase (LDH) leakage, lysosomal pH change, nicotinamide adenine dinucleotide hydride (NADH) content, adenosine triphosphate (ATP) level, and ROS generation, respectively.

These interactions of MeONPs with cells may lead to cytokine release and affect cell–cell communications such as the recruitment of immune cells and proliferation of profibrogenic cells. We measured the release of pro-inflammatory cytokines (TNF-α, IL-1β, IL-2, IL-6, and MCP-1) by THP-1 cells and growth factor (TGF-β1) by BEAS-2B cells. For a snapshot view of the results, the measured levels of descriptors in cells incubated with 0–200 μg/mL MeONPs were ranked into three

levels, leading to a visual display where high, moderate, and negligible effects are represented by red, yellow and blue colors, respectively. Figure 2A and Fig. S2 show the effects of ten representative MeONPs in THP-1 and BEAS-2B cells, respectively, while the others are listed in Supplementary Data 3. Fifteen branch events were quantitatively measured for the 52 MeONPs at five different exposure concentrations (12.5, 25, 50, 100, 200 μg/mL), resulting in 75 input parameters (Supplementary Data 3). Additionally, four descriptors were collected from the interactions between MeONPs and two biological media (SLF and PSF), and eight descriptors were acquired from the periodic table (Supplementary Data 1). These data allowed us to establish a multimodal database consisting of 87 input parameters in total (Table 1). As MeONPs were dispersed in cell culture media, protein coronas could potentially form on their surface. This phenomenon resulted in minimal interference from MeONPs themselves on the bioanalytical results, with relative errors consistently below 5% (Supplementary Data 2), suggesting high accuracy of the detected in vitro parameters.

Mice were exposed to the 52 MeONPs via oropharyngeal aspiration to collect toxicological endpoints in vivo to assess their fibrogenic effects. Figure 2B illustrates the workflow of the animal experiments. The animals were subjected to three exposures to MeONP suspensions during the first 3 weeks and were sacrificed on day 90 to collect BALF and lung tissues for further examination, adhering to the subchronic inhalation toxicity study guideline recommended by the Organization for Economic Co-operation and Development (OECD)[48].

In the pathogenic process of lung fibrosis, active TGF-β1 plays a critical role in promoting fibroblast proliferation to secrete collagens. We, therefore, quantified the release of active TGF-β1 in BALF by ELISA and visualized collagen deposition by Masson's trichrome staining of lung sections. Collagen staining images acquired from 203 whole slide images of lung sections were assessed by the Ashcroft score, a widely used index to rank pulmonary fibrosis (Fig. 2C). Figure 2D shows the expression levels of TGF-β1 in BALF and the Ashcroft score of mouse lungs exposed to ten representative MeONPs. The fold change of TGF-

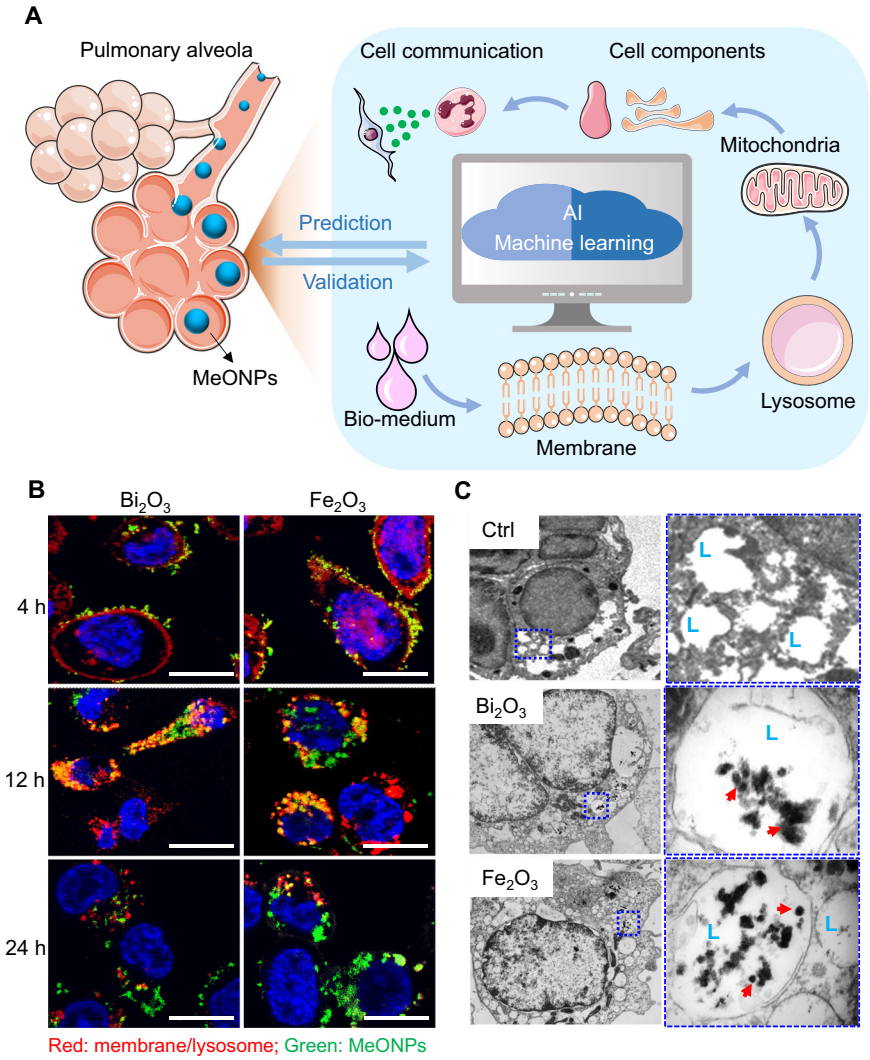

Fig. 1 | Interfaces of nano-bio interactions in the lungs. A Schematic workflow of multimodal feature fusion (MFF) modeling. The figure depicts the travel path of nanoparticles in lungs where inhaled nanoparticles may deposit in alveoli and interact with macrophages and epithelial cells, leading to injury of various cellular components such as cell membranes, lysosomes, mitochondria, and other cellular components. Descriptive features at these nano-bio interfaces and fibrogenic indexes in vivo were collected to develop predictive models using machine learning methods. The established in silico model was further validated by animal tests. The cell and tissue elements were adapted and modified from figures provided by Servier Medical Art, licensed under a Creative Commons Attribution 4.0 Unported License (https://creativecommons.org/licenses/by/4.0/). **B** Confocal and **C** TEM imaging of MeONPs in cells. THP-1 cells exposed to 12.5 μg/mL FITC-labeled or pristine MeONPs were collected. The fixed cells were stained with DAPI (blue) and Alexa Fluor™ 594 conjugated with WGA/anti-LAMP1 (red) for confocal imaging. Scale bar = 15 μm. Arrow and L indicate the MeONP and lysosome, respectively.

https://doi.org/10.1038/s41467-025-58016-w

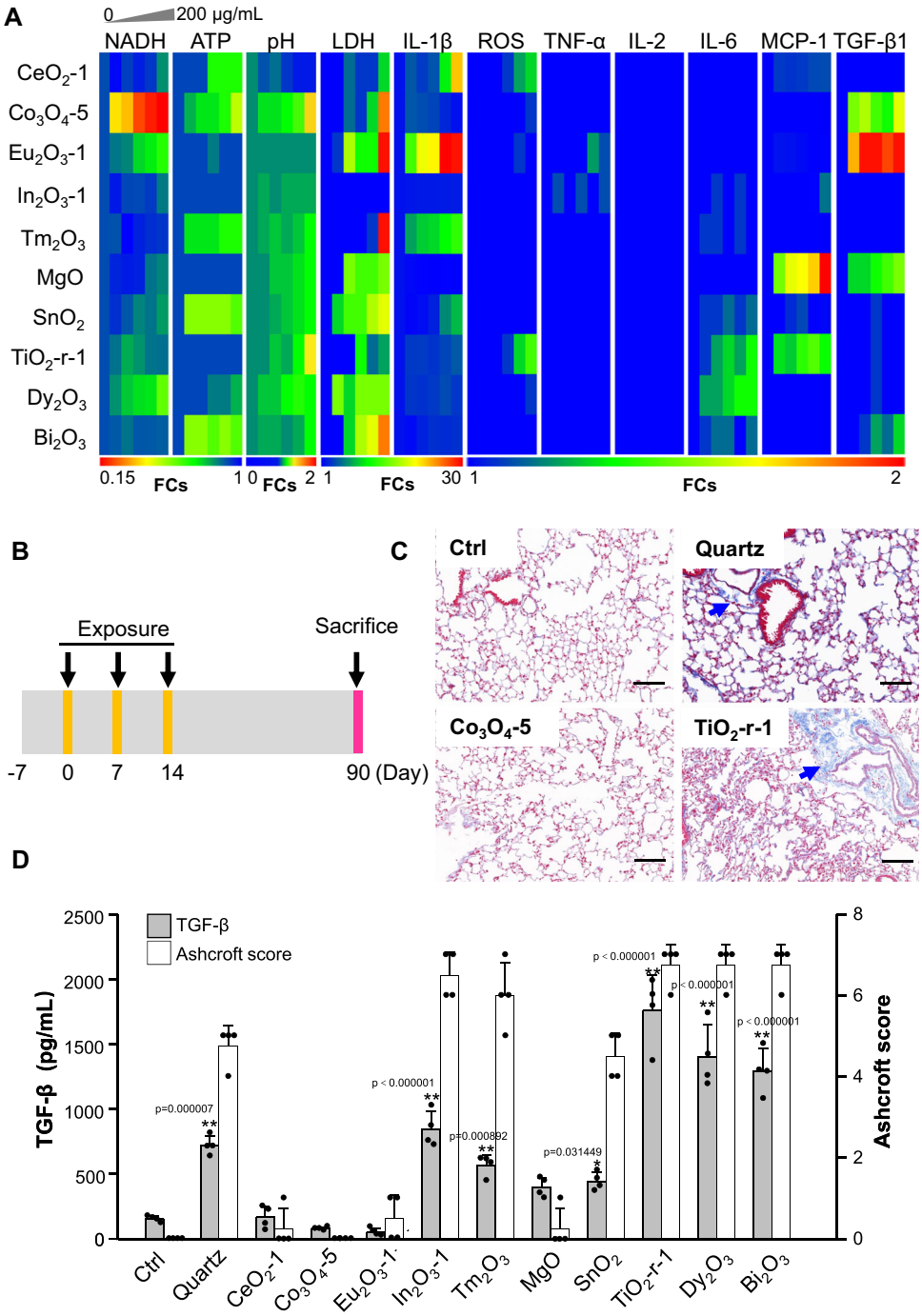

Fig. 2 | Effects of representative MeONPs in cells and mouse lungs. A Heatmap displaying the impacts of 10 representative MeONPs on THP-1 and BEAS-2B cells by detecting LDH leakage, ROS generation, NADH content, lysosomal pH change, ATP production, and cytokine release. THP-1 cells were exposed to 0, 12.5, 25, 50, 100, and 200 μg/mL MeONPs for 24 h, followed by LDH and cytokine measurement in supernatants and ROS, NADH, ATP, and lysosomal pH detection in cells. BEAS-2B cells were exposed to 0, 12.5, 25, 50, 100, and 200 μg/mL MeONPs for 24 h, followed by TGF-β1 detection in cells. The values of these descriptors in MeONP treatments were compared with control cells. The resulting ratios were expressed as fold changes (FCs) in the heatmap. **B** Schematic illustration of MeONP instillation in mice. Mice were oropharyngeally administered with 50 μL PBS (vehicle control), 2 mg/kg MeONPs, and quarts (positive control) three times a week. The animals were sacrificed on day 90 to collect BALF and lung tissues for further examinations. **C** Masson's trichrome staining of lung tissues exposed to representative MeONPs. Scale bar = 50 μm. **D** TGF-β1 release in BALFs and Ashcroft score of stained lung sections. Data were presented as means ± SD. BALFs were collected to measure TGF-β1 by ELISA ($n = 4$). $^{*}p < 0.05$, $^{**}p < 0.01$, and $^{***}p < 0.001$ compared to the vehicle control by one-way ANOVA. Source data are provided as a Source Data file.

β1 ($FC_{TGF-β1}$) and collagen staining images of the 52 MeONPs are shown in Supplementary Data 4 and Fig. S3, respectively.

Among the 52 tested MeONPs, 23 (Fe_2O_3-4, TiO_2-r-1, TiO_2-r-2, TiO_2-a-1, TiO_2-a-2, TiO_2-a-3, α-Al_2O_3, γ-Al_2O_3-1, γ-Al_2O_3-2, Dy_2O_3, NiO-1, In_2O_3-1, In_2O_3-2, Tm_2O_3, Tb_2O_3, Bi_2O_3, Sm_2O_3, Y_2O_3, Yb_2O_3, Sb_2O_3, SnO_2, CuO-3 and ZnO-1) consistently induced high levels of TGF-β1 with $FC_{TGF-β1}$ ≥2 and significant collagen deposition, 11 (CeO_2-2, α-MnO_2-1, CuO-2, CuO-4, NiO-2, MgO, MoO_3, ZnO-2, ZnO-3, Fe_2O_3-2 and Fe_2O_3-3) had a moderate effect, and 18 (CeO_2-1, CeO_2-3, Co_3O_4-1, Co_3O_4-2, Co_3O_4-3, Co_3O_4-4, Co_3O_4-5, α-MnO_2-2, α-MnO_2-3, Eu_2O_3-1, Eu_2O_3-2, Cr_2O_3, Gd_2O_3, Nd_2O_3, Er_2O_3, La_2O_3, CuO-1, and Fe_2O_3-1) showed similar levels of cytokine release and collagens to the vehicle

Table 1 | Multimodality input parameters

Type	Descriptors	Number
Periodic parameters	Molecular weight	1
	Electronegativity of metal atom	1
	Metal atom number	1
	Oxygen atom number	1
	Cation charge	1
	Periodic number of metal atom	1
	Group number of metal atom	1
	Atomic ratio of metal and oxygen	1
Physicochemical properties in biological fluids	Hydrodynamic size	1
	Zeta potential	1
	Dissolution in PSF	1
	Dissolution in SLF	1
MeONP-membrane interaction	LDH release in THP-1 cells	5
	LDH release in BEAS-2B cells	5
MeONP-lysosome interaction	pH changes in lysosomes	5
Impact on mitochondria activity	NADH level in THP-1 cells	5
	NADH level in BEAS-2B cells	5
	ATP level in THP-1 cells	5
	ATP level in BEAS-2B cells	5
Impact on redox-homeostasis	ROS generation in THP-1 cells	5
	ROS generation in BEAS-2B cells	5
Impact on cell–cell communications	TNF-α release in THP-1 cells	5
	IL-1β release in THP-1 cells	5
	IL-2 release in THP-1 cells	5
	IL-6 release in THP-1 cells	5
	MCP-1 release in THP-1 cells	5
	TGF-β1 release in BEAS-2B cells	5
Total descriptors		87

control. Notably, four MeONPs had differing effects on TGF-β1 and collagen deposition: MgO, MoO_3, ZnO-2, and ZnO-3 induced high TGF-β1 release, but had little effect on collagen deposition with an Ashcroft score <2.

Among all tested MeONPs, we identified six sets of similar nanoforms, consisting of three fibrogenic groups (Al_2O_3, In_2O_3, and TiO_2) and three non-fibrogenic groups (CeO_2, Eu_2O_3, and Co_3O_4). The parameter boundaries defining these nanoforms are presented in Supplementary Data 6. The recognition of these similar nanoforms could significantly simplify the fibrogenic risk assessment of other Al_2O_3, In_2O_3, TiO_2, Eu_2O_3, CeO_2, and Co_3O_4-based nanoforms falling within these parameter boundaries, potentially eliminating the need for additional biological assessments for fibrogenic potentials by read-across strategies[49].

A correlation analysis with 12 conventional *in chemico* descriptors (in Table 1) did not reveal straightforward relationships between observed fibrogenic effects and these traditional descriptors. This outcome emphasizes the intricate nature of nano-bio interactions, suggesting that the variations in MeONP-induced pulmonary fibrosis cannot be solely attributed to commonly considered physicochemical properties. In light of this complexity, it is imperative to explore additional, perhaps more nuanced, physicochemical properties of MeONPs that might play a crucial role in influencing their biological effects. This perspective underscores the need for a comprehensive understanding of the multifaceted factors contributing to MeONP-induced pulmonary fibrosis.

A fibrogenic tag was assigned to an animal when $FC_{TGF\text{-}\beta1} \geq 2$ or Ashcroft score ≥2, while a non-fibrogenic tag was assigned otherwise (Fig. S4). This labeling system resulted in an assembly of fibrogenic and non-fibrogenic tags, collectively termed in vivo datapoints. A datapoint is consistently represented as each individual mouse. In contrast, input parameters/descriptors are comprised of specific values obtained from either the periodic table or bioanalytic assays. Given that each MeONP was tested in four mice, theoretically, 208 mice across 52 MeONP treatments should yield 208 in vivo datapoints. However, five animals in the Co_3O_4-1 (training set), Co_3O_4-2 (training set), Eu_2O_3-2 (training set), Gd_2O_3 (training set), and Co_3O_4-3 (test set) treatments were excluded due to antibiotic administration to treat wounds resulting from conflicts with other mice. Consequently, among the 203 remaining in vivo datapoints, 126 were identified as fibrogenic and 77 were non-fibrogenic (Supplementary Data 5). The ratio of fibrogenic to non-fibrogenic MeONP was 1.6:1. For each in vivo datapoint, there were 87 associated input parameters for multimodal feature fusion (MFF) analysis.

Machine learning modeling in the MFF predictive framework

Given the complexity of the 15 branched events involved in the interactions of MeONPs with membrane, lysosome, mitochondria, redox-homeostasis, and cell-cell communication signals (Table 1), machine learning methods were selected to establish the predictive framework. An MFF predictive framework driven by machine learning was proposed to identify meaningful patterns between heterogeneous multi-dimensional events and lung fibrosis in animals. To identify a suitable machine learning algorithm for the database, models were developed and evaluated using eight algorithms, including random forest (RF), locally weighted learning (LWL), C4.5 decision tree (DTr), k-nearest neighbor (*k*-NN), support vector machine (SVM), Bayesnet, decision table (DTa), and logistic regression (LGR). The dataset was randomly split into a training set containing 156 data points of 40 MeONPs and a test set consisting of 47 data points generated from 12 MeONPs. The training set was further randomly split ten times to acquire the average performance, known as tenfold cross-validation. The six performance metrics values of the eight machine learning algorithms in the tenfold cross-validation on the training set and in the external validation on the test set are plotted in Fig. 3. Their detailed performances (ACC, MCC, SE, SP, AUC, and F1 values) of the eight algorithms are provided in Supplementary Data 7. The formulae of the indexes (ACC, MCC, SE, SP, AUC, and F1 values) are listed in the supporting information. Among all models, the RF model had the best performance, with a strong robustness (ACC = 89% and AUC = 94% in the tenfold cross-validation) and a high predictive accuracy (ACC = 84% and AUC = 85% in the external validation). The models developed with DTr, SVM, and Bayesnet also exhibited a satisfactory performance, with *ACC* values of 85–90% in the tenfold cross-validations and 74–76% in the external validations. Their AUC values ranged from 84 to 90% in the cross-validations and 61 to 79% in the external validations. However, the remaining four classifiers showed poor performance in the external validations. The ACC values were below 70% for *k*-NN, DT, and LGR models, and the AUC for the LWL model was less than 40%. Based on these results, RF was selected as the optimal algorithm for the MFF predictive framework. Thus, the RF model was further validated by animal tests.

The number of data points used for training and testing the predictive models is relatively small compared to some modeling studies on chemicals. However, there is not much room for expanding the number of MeONPs used in modeling because of the restrictions on MeONP sources. Compared to the reported modeling studies with 17–30 nanoparticles[10,37,38], the dataset built here is the largest to our best knowledge. We believe that with the increase in the synthesis of new MeONPs and the amount of toxicity data, the performance of the model will be further improved in the future.

https://doi.org/10.1038/s41467-025-58016-w

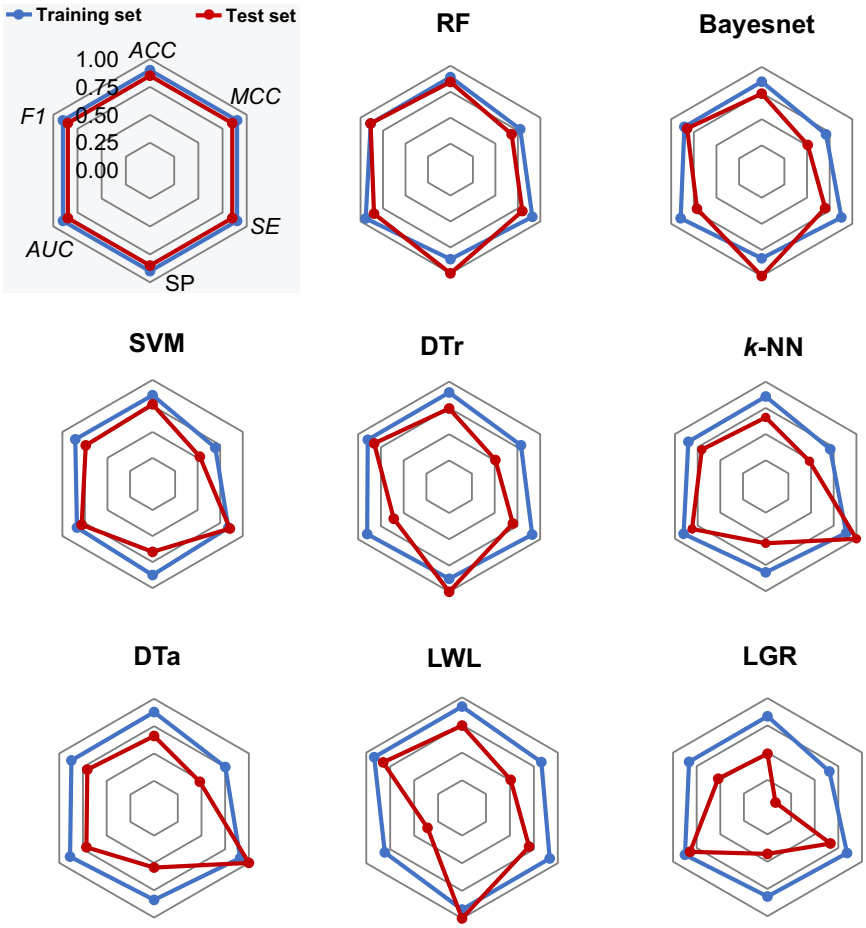

Fig. 3 | Performance of models constructed using eight machine learning algorithms. The y-axis represents the values of the performance metrics. RF random forest, DTr C4.5 decision tree, LWL locally weighted learning, *k*-NN k-nearest neighbor, SVM support vector machine, DTa decision table, LGR logistic regression. ACC overall predictive accuracy, MCC Matthews correlation coefficient, SE sensitivity, SP specificity, AUC the area under the receiver operating characteristic curve, F1 F1 score. Source data are provided as a Source Data file.

Experimental validation of the MFF predictive model

Five new MeONPs (Ho_2O_3, Pr_6O_{11}, Co_3O_4, ZrO_2, and CuO) not included in the training or test sets were selected for validation ($n = 4$ for each MeONP). These selected MeONPs were administered to 20 mice for 90 days, and the extent of fibrosis was determined by measuring TGF-β1 in BALF (Fig. S5A) and collagen deposition in lung tissues (Fig. S5B). The resulting 20 datapoints (positive/negative ratio = 1:1.86) from the animal tests were then compared to the predictions generated by the MFF models (Supplementary Data 8). A datapoint consistently represents a fibrogenic ranking tag from each individual mouse. The models exhibited high predictive accuracy for this independent dataset of lung fibrosis, achieving an ACC of 85% and AUC of 98%. As shown in Fig. 4A, 17 out of the 20 datapoints were accurately predicted, primarily for Ho_2O_3, Pr_6O_{11}, Co_3O_4, and ZrO_2. The remaining three datapoints generated from CuO were correctly predicted in terms of collagen staining but not TGF-β1 levels.

We further assessed the applicability domain and diversity of the validated MEF model. These two characteristics are crucial for ensuring the inclusion of representative data and defining the range within which the proposed framework can be reliably applied for new MeONPs. To characterize the applicability domain, we employed a descriptor standardization approach, which encompassed all 223 datapoints from the training set (156), test set (47), and experimental validation set (20) (Supplementary Data 9). The descriptors were normalized according to a reported descriptor standardization approach[50]. Taking IL-1β as an example, the normalization process involves two steps. First, the average (Avr) and standard deviation (SD) of IL-1β for all tested MeONPs were calculated. Then, the normalized value was calculated using the formula:

$$\text{Normalized IL} - 1\beta = \left|\frac{X - \text{Avr}}{\text{SD}}\right| \quad (1)$$

where X is the IL-1β value for a specific MeONP at a certain concentration. Overall, seven descriptors, including IL-1β, NADH in macrophages, TGF-β1, dissolution in PSF, zeta potential, hydrodynamic size, and NADH in epithelial cells, were normalized.

We generated a similarity network of the 223 datapoints and their seven descriptors using Gephi software (V 0.9). The data were presented as nodes and colored according to the chemical composition of MeONPs. We used the size of the circle to represent the fibrosis level (release of TGF-β1) in the lung. The thickness of the lines reflected the strength of the correlations between nodes calculated based on their seven descriptors. Frequent and sparse connections indicated high and low homogeneity of the data in descriptor space consists of in vitro and *in chemico* parameters, respectively. Notably, the descriptor space of MeONPs exhibited significant heterogeneity, with datapoints scattered widely.

Mechanism interpretation

We attempted to interpret the mechanism by analyzing the key biological events associated with MeONP-induced lung fibrosis. A Shapley

https://doi.org/10.1038/s41467-025-58016-w

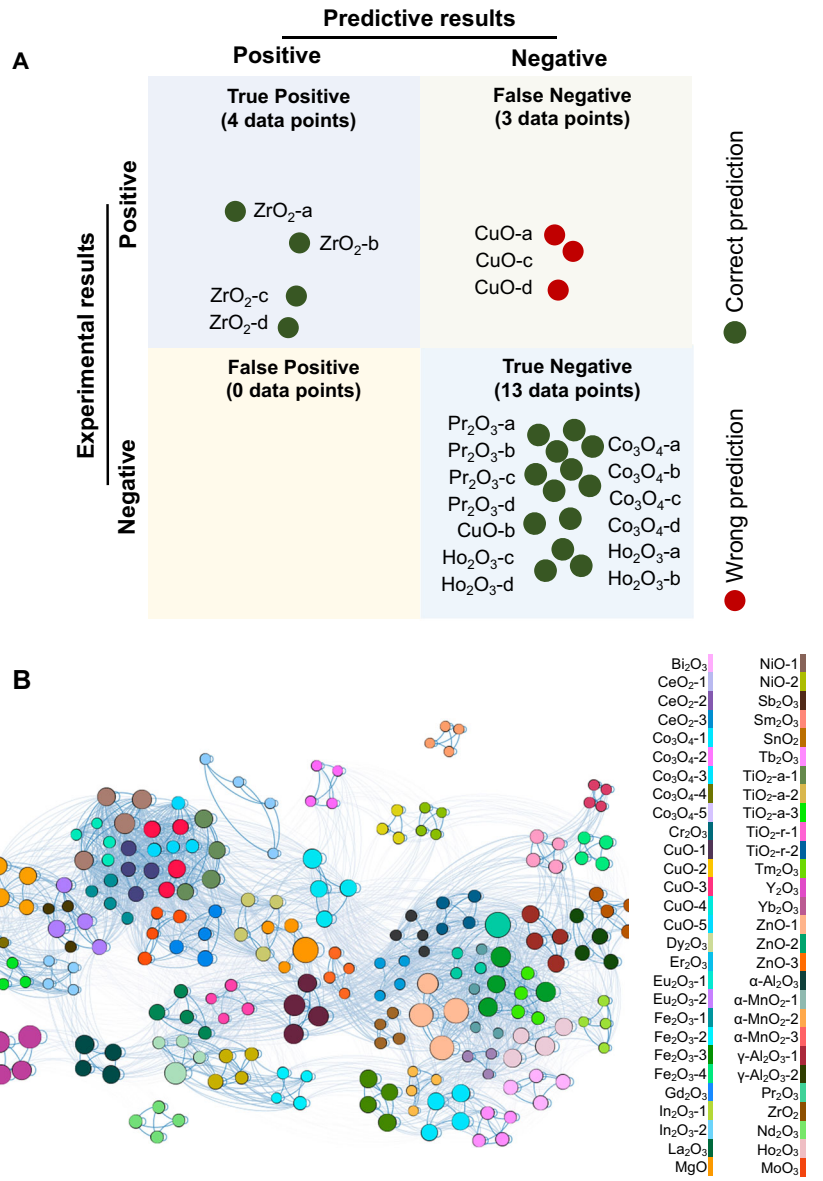

Fig. 4 | Experimental validation and diversity analysis of the established model. **A** Experimental and predicted results of lung fibrosis in the experimental validation set are depicted in the confusion matrix, with each node representing a datapoint. **B** Distribution of the 223 datapoints (156 in the training set, 47 in the test set, and 20 in the experimental validation set) in the similarity network. Each node represents a datapoint which is colored according to the chemical composition of MeONPs. The size of a node indicates the fibrosis level in the lung, while the thickness of a line represents the strength of correlation between the two connected nodes. Frequent and sparse connections denote high and low homogeneity of nodes for descriptor spaces, respectively.

Additive Explanation plot (SHAP) plot was used to identify the features that exert significant influence. Figure 5A illustrates the SHAP summary plot, where each dot represents individual data in the dataset. The horizontal position of the dots on the x-axis indicates the impact of the corresponding feature values on the model's predictions. The top seven features that exert the greatest influence on the model's predictions are IL-1β, NADH in macrophages, TGF-β1, dissolution in PSF, zeta potential, hydrodynamic size, and NADH in epithelial cells. Notably, IL-1β emerges as the most critical descriptor, contributing 27.8% to the overall feature importance, followed by NADH in THP-1 at 17.6%. The remaining five descriptors accounted for 54.5% of the feature importance (Fig. 5B).

Based on the results of the SHAP analysis, we sought to elucidate the mechanisms underlying MeONP-induced lung fibrosis. As illustrated in Fig. 5C, the mucociliary escalator efficiently clears large MeONP agglomerates from the airways. However, smaller particles, particularly cationic ones, can penetrate the LLF, interacting with macrophages or epithelial cells and subsequently entering lysosomes for decomposition. Subsequently, the released metal ions or escaped MeONPs can interact with mitochondria, disrupting cellular metabolism and eliciting ROS, leading to the activation of IL-1β and TGF-β1. These cytokines, in turn, promote the recruitment of immune cells, proliferation of fibroblasts, and deposition of collagen, culminating in the development of pulmonary fibrogenesis. Notably, these key events have been well documented in the literature regarding fibrosis pathology and the pulmonary behavior of nanoparticles[25,51].

We conducted additional experiments to validate the interpreted mechanisms, focusing particularly on the top two contributing factors identified by SHAP values: IL-1β and TGF-β1.To elucidate the impact of these factors, we implemented a coculture system involving THP-1, BEAS-2B, and Wi-38/VA-13 cells, representing essential cellular components in the progression of lung fibrosis (Fig. 6A). α-Al_2O_3, identified as significant inducers of lung fibrosis in animal models, was incubated in this system. As a point of comparison, a non-fibrogenic MeONP

(Fe_2O_3-1) and a conventional fibrogenic material (Quartz) were included. Within this coculture system, we measured fibroblast proliferation. Figure 6B demonstrates that α-Al_2O_3 induced substantial increases in the metabolic viability of fibroblasts, similar to the effect of Quartz, while Fe_2O_3-1 had a minimal effect. Newborn cell staining images indicate that the α-Al_2O_3-induced fibroblast viability increase could be attributed to the rise in the number of newborn cells (Fig. 6C).

To further validate the roles of IL-1β and TGF-β1 in the fibrosis progression, we employed siRNA against IL-1β (siIL-1β) and TGF-β1 (siTGF-β1) to establish THP-1^{KD} and BEAS-$2B^{KD}$ cells, respectively. Remarkably, the introduction of THP-1^{KD} or BEAS-$2B^{KD}$ cells significantly attenuated α-Al_2O_3 induced fibroblast proliferation. These experimental results provide concrete evidence supporting our initial findings regarding the crucial roles of IL-1β and TGF-β1 in MeONP-induced lung fibrosis. These results enhance the robustness and validity of our mechanistic interpretations.

While we used TGF-β1 in BALF and Ashcroft scores of histology images in this study due to the limited availability of reliable non-animal classifiers for lung fibrosis, we acknowledge the importance of exploring non-animal alternatives for classification, aligning with the principles of the 3Rs (Replacement, Reduction, Refinement) in animal testing. In our research, the in silico model was constructed using a combination of *in chemico* and in vitro data, showcasing a step toward non-animal methods for predictive modeling. As the number of ENMs continues to expand, it is crucial to evaluate their potential profibrogenic risks before exposure to the environment. MFF has demonstrated high predictive accuracy in assessing the fibrogenic risk of MeONPs. To improve the practicality of the MFF model, it was transformed into a software named "Nano-induced lung fibrosis prediction" (NILFP v 1.0.0) with a simplified user interface. It is available for non-commercial use at GitHub (https://github.com/huangyang2023/NILFPv1.0.0). NILFP can be used for fibrogenic risk assessment of untested MeONPs, MeONP-based nanoproducts, and beyond by using three *in chemico* descriptors (hydrodynamic size, zeta potential, and dissolution degree in PSF) and four in vitro descriptors, including IL-1β in supernatants of THP-1 cells exposed to 12.5 μg/mL MeONPs, viability of THP-1 cells exposed to 200 μg/mL MeONPs, and viability and secreted TGF-β1 in BEAS-2B cells exposed to 25 μg/mL MeONPs (Fig. S6). The robust predictive capability of our in silico model can be attributed to: (i) the careful selection of critical nano-bio interactions based on the biological fate of MeONPs in the lungs; (ii) the use of relevant cell models tailored to study lung fibrosis; (iii) the integration of *in chemico* and in vitro data, providing a comprehensive representation of the dynamics underlying lung fibrosis.

Within the complex milieu of LLF, composed of various lung surfactants and proteins, a surface corona may form on the particle surface, influencing their biological fate upon MeONP penetration through the LLF[52,53]. While pre-coating nanoparticles with LLF could better align with the travel path of MeONPs, the practical implementation of this is challenging. This challenge arises from the lack of convincing techniques for collecting natural LLF in vivo or creating artificial fluids that faithfully replicate the composition of natural LLF. In our study, MeONPs were dispersed in cell culture media to form a protein corona. However, upon entry into cell lysosomes, the acidic and enzymatic environment of lysosomal fluids may accelerate the degradation of surface corona and the dissolution of MeONPs.

Given the widespread use of MeONPs for various applications such as coloring, bacterial killing, and coating in industries and daily life, the potential inhalation exposure to fine particulates of metal oxides poses significant risks. Airborne concentrations of MeONPs have been reported to reach notable levels in the workroom and ambient air. For example, airborne TiO_2, Fe_2O_3, and Al_2O_3 have been measured at 7.6[54], 1.9[55], and 1.4 mg/m^3 [56], respectively. Employing a calculation approach recommended by NIOSH[51,57], it is estimated that continuous exposure of workers to 7.6 mg/m^3 MeONPs for 8 h a day over 10 months and 5 years could result in a lung burden high up to 1.9 mg/m^2. NIOSH calculation indicates that a bolus exposure of 1 mg/kg in a mouse is equivalent to 0.5 mg/m^2 of nanoparticle exposure in mouse lungs. Oropharyngeal aspiration of 2 mg/kg MeONPs in mice, as employed in our in vivo experiments, is therefore comparable to potential occupational exposure scenarios. Moreover, we attempted to mirror these conditions in our in vitro assays. Assuming a homogeneous distribution of MeONPs in a tissue culture dish and a 10-μm thickness of the cell layer, the corresponding in vitro doses used in this study should be less than 200 μg/mL. We deliberately selected a wide in vitro dose range from 12.5 to 200 μg/mL because this range allows us to acquire more input descriptors, facilitating the identification of predictive indexes at specific MeONP doses.

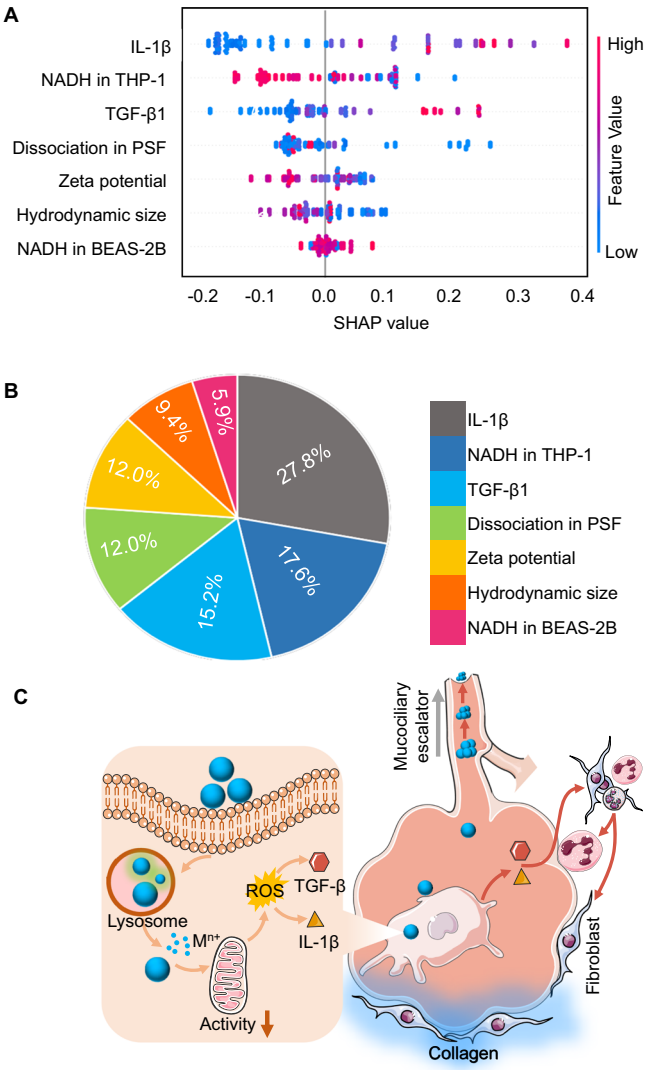

Fig. 5 | Identification of key descriptors for mechanism interpretation. A SHAP summary plots displaying the effects of features and their values on the prediction. The y-axis of each plot contains the features included in the model sorted from the most (top) to least (bottom) important. The x-axis depicts the SHAP value, with each point referring to a SHAP value associated with a value of a certain feature. The color of the point displays whether the feature value is high (pink) or low (blue). **B** Feature importance in the RF model. **C** Schematic image of the proposed *in chemico*/in vitro-in vivo extrapolation of lung fibrosis. The key determinants of MeONP-induced lung fibrosis include IL-1β, TGF-β1, metabolic activity, hydrodynamic size, zeta potential, and metal ion release in PSF. Source data are provided as a Source Data file. The cell and tissue elements were adapted and modified from figures provided by Servier Medical Art, licensed under a Creative Commons Attribution 4.0 Unported License (https://creativecommons.org/licenses/by/4.0/).

https://doi.org/10.1038/s41467-025-58016-w

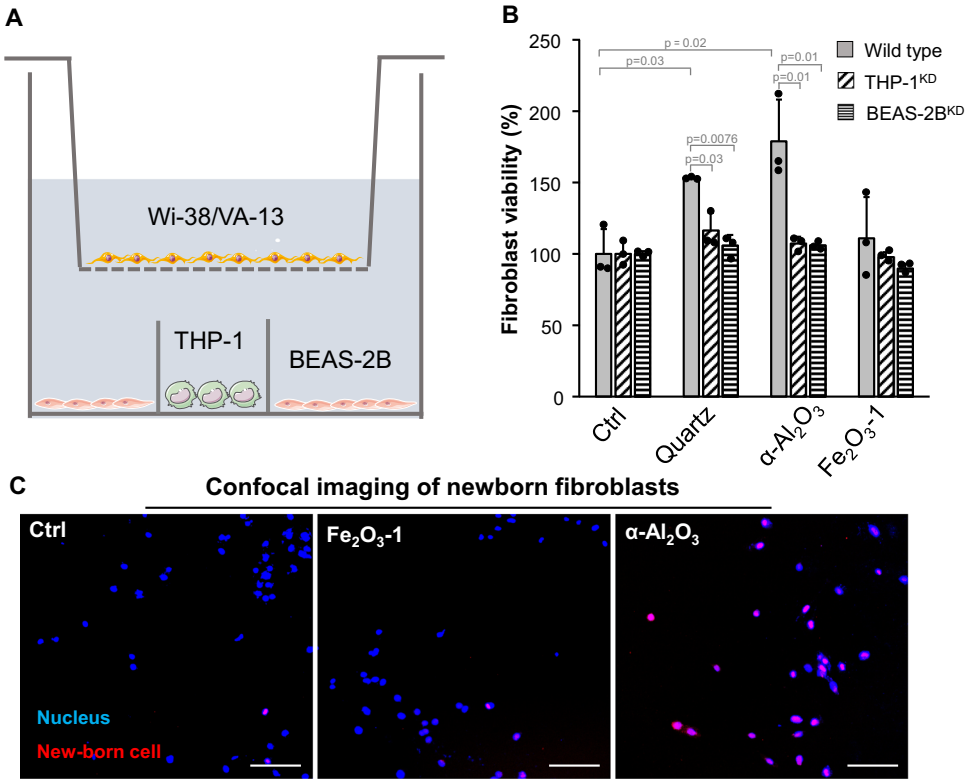

Fig. 6 | Assessment of fibroblast proliferation in a coculture system. **A** Schematic image showing the construction of a coculture system and assessment of fibroblast proliferation by The cell elements were adapted and modified from figures provided by Servier Medical Art, licensed under a Creative Commons Attribution 4.0 Unported License (https://creativecommons.org/licenses/by/4.0/). **B** viability test ($n = 3$) and **C** newborn cell imaging. In the coculture setup, THP-1/THP-1^{KD} cells were seeded inside the Oxford ring of the lower chamber of transwell plates at a density of 1×10^4 cells/well. BEAS-2B/BAEAS-2B^{KD} cells were seeded in the outer area of the Oxford ring in the lower chamber at 3×10^4 cells/well. Wi-38/VA-13 cells were seeded in the upper chamber of transwell plates at 2×10^3 cells/well. The cells were exposed to 50 μg/mL MeONPs or 12.5 μg/mL quartz for 24 h. Subsequently, the proliferation of Wi-38/VA-13 cells was examined using the MTS assay and newborn cell imaging. Scale bar = 200 μm. The cell viability results are shown as means ± SD. $^*p < 0.05$ compared to Ctrl, $\#p < 0.05$, $\#\#p < 0.01$ compared to Wild-type cells by two-tailed Student *t*-test. Source data are provided as a Source Data file.

Big data analysis prefers a large set of data points. This contributes to the increased model robustness, improved generalization to new data, and an enhanced ability to capture complex patterns and interactions within the data. Larger datasets can also reduce the risk of overfitting, leading to more accurate and reliable predictions. We acknowledge that the number of data points (203) for 52 MeONPs is relatively small compared to some machine learning models applied to conventional chemical molecules[58–60]. However, there is limited room for expanding the animal datapoint number under current research conditions due to the absence of reliable sources to collect more MeONPs and the ethical restrictions for the overuse of animals in each treatment. Despite these limitations, our predictive model demonstrates good robustness and reliability because of the use of high-quality data acquired from strictly controlled experiments with consistent experimental protocols. In addition, we employed tenfold cross-validations and external validation in data analysis to ensure the robustness and predictive accuracy of our model.

Our study presents a reliable in silico model for predicting the fibrogenic potential of ENMs through the construction of an MFF predictive framework. The MEF model achieved high accuracy (>85%) in predicting MeONP-induced lung fibrosis, making it a valuable tool for risk assessment. The developed model was applicable to different MeONPs. Our machine learning analysis revealed seven key descriptors, comprising three *in chemico* descriptors (dissolution in PSF, zeta potential, and hydrodynamic size) and four in vitro descriptors (IL-1β, NADH in macrophages, TGF-β1, and NADH in epithelial cells). These descriptors enabled the prediction of ENM-induced lung fibrosis by combining abiotic characterization and in vitro assays, thereby obviating the need for animal experiments. The established predictive framework may serve as an initial paradigm for the identification of fibrogenic nanomaterials, facilitating their further grouping through read-across strategies. Overall, our research provides a cost-effective, time-efficient, and mechanism-driven alternative to the current practice of chronic nanotoxicity assessment in animals.

Methods

Ethics

All animal experiments were approved by the Ethics Committee of Soochow University (Approval NO. 202108A0167). Animals were housed in groups of four under standard laboratory conditions (25 °C; 60% relative humidity; 12 h light, 12 h dark cycle) and hygiene status (autoclaved food and acidified water) according to Soochow University guidelines for the care and treatment of laboratory animals.

Materials

MTS and ATP assay kits were obtained from Promega (Madison, WI, USA). H_2DCF-DA, Fetal bovine serum (FBS), penicillin, and streptomycin were obtained from Thermo Fisher Scientific (Grand Island, NY, USA). RPMI 1640 medium was purchased from Corning (Steuben, NY, USA). Bronchial epithelial cell medium was purchased from ScienCell (San Diego, CA, USA). ELISA kits for detection of IL-1β, IL-2, IL-6, IL-12, and TNF-α were from BD biosciences (San Jose, CA, USA). ELISA kits for the detection of TGF-β1 came from RD biotechne (MN, USA). LDH assay kits were obtained from Leagene (Beijing, China). LysoSensor™ Yellow/Blue DND-160 was purchased from Yeasen Ltd. (Shanghai, China). 4% paraformaldehyde was obtained from Biosharp (Anhui,

China). Al_2O_3, TiO_2, ZnO, NiO, In_2O_3, Bi_2O_3, ZrO_2, MoO_3, SnO_2, MgO, Sb_2O_3, CeO_2-1, CeO_2-2, Y_2O_3, Dy_2O_3, and Yb_2O_3 were obtained from Aladin (Shanghai, China). The rest of the materials were made in the laboratory. Comprehensive details regarding the sources and original synthesis of the MeONPs can be referenced in Supplementary Data 1.

Material characterization

Morphologies and primary sizes of MeONPs were examined by transmission electron microscopy (TEM) using a Tecnai G2 spirit BioTwin microscope (FEI, Oregon, USA) operated at 120 kV. MeONP suspensions (50 μg/mL in deionized water) were placed on 200-mesh copper grids coated with carbon-coated formvar support film (Ted Pella, Inc., Redding, CA, USA) and air-dried at room temperature. The hydrodynamic diameters and surface charges of MeONP dispersions in water were determined by dynamic light scattering and zeta potential analysis using a Zetasizer Nano ZS90 instrument (Malvern Instruments Corp., UK), as previously described[10]. A Limulus Amebocyte Lysate assay was conducted on these MeONPs to assess endotoxin contaminations according to the manufacturer's protocol. All MeONPs showed negative results in the endotoxin test (Supplementary Data 10).

Preparation of MeONP suspension

The MeONP suspensions were acquired by sonication[7,61]. In detail, the stock solution (5 mg/mL) of MeONPs in DI H_2O were dispersed by a water-bath sonication for 15 min. Then, the stock solutions were diluted to the desired concentrations in 5 mL Eppendorf tubes containing complete cell culture media, PBS, PSF, or SLF. The diluted MeONP solutions were further dispersed by probe sonication at 32 W for 10 s. The MeONP suspensions were then immediately subjected to physicochemical property characterizations, cell incubations, or animal exposure.

Examination of metal dissolution in simulated biological fluids

To investigate the dissolution behavior of MeONPs in PSF and SLF, MeONP stock solution (5 mg/mL) was dissolved in 10 mL of PSF buffer (142 mg/L Na_2HPO_4, 6.65 g/L NaCl, 62 mg/L Na_2SO_4, 29 mg/L $CaCl_2{\cdot}H_2O$, 250 mg/L glycine, 8.09 g/L potassium phthalate, pH 4.5) or SLF buffer (95 mg/L $MgCl_2$, 6.019 g/L NaCl, 298 mg/L KCl, 126 mg/L Na_2HPO_4, 63 mg/L Na_2SO_4, 368 mg/L $CaCl_2{\cdot}2H_2O$, 574 mg/L CH_3COONa, 2.604 g/L $NaHCO_3$, 97 mg/L sodium citrate dihydrate, pH 7.4) at a concentration of 50 μg/mL with probe sonication at 32 W for 10 s. The resulting MeONP suspensions were incubated for 24 h at room temperature. After that, the MeONP suspensions underwent centrifugation at 15,000 rpm for 10 min, and 5 mL of supernatants were collected. To assess the dissolution percentage, the supernatants were subjected to digestion using an acid mixture, following a previously reported method[62]. The resulting digestion solution was subjected to metal ion detection by inductively coupled plasma-atomic emission spectrometry (ICP-OES DUO 6500, Thermo Scientific, Massachusetts, USA). The percentage of MeONP dissolution was calculated using the following equation:

$$\text{Dissolution}\% = \frac{C_t \times V_t}{C_0 \times V_0 \times R} \times 100\% \quad (2)$$

where C_0 is set at 50 μg/mL, representing the mass concentration of MeONPs in nanoparticle suspensions; C_t represents the mass concentration of metal ions in the digestion solution of supernatants separated from MeONP suspensions. V_0 is the volume of MeONP suspensions, equal to the volume (5 mL) of supernatant. Vt is the volume of the digestion solution for ICP-OES analysis; R represents the mass ratio of metal elements in each specific MeONP.

Assessment of in vitro toxicity

THP-1 (catalog number: TIB-202) and BEAS-2B (catalog number: CRL-3588) cells obtained from ATCC were cultured in RPMI 1640 medium supplemented with 10% fetal bovine serum (Gemini) and BEpicM (Sciencell), respectively. Authentication of THP-1 cells involved immunostaining for Complement (C3)/Fc, while BEAS-2B cells were authenticated through immunostaining for keratins. Additionally, prior to experimental use, we ensured the validation of cell morphologies in accordance with the guidelines provided by ICLAC. To assess the effects of MeONPs, THP-1 cells were primed with 1 μg/mL PMA and seeded in 96-well plates at a density of 3×10^4 cells/well. BEAS-2B cells were seeded in plates at a density of 8×10^3 cells/well. After overnight culture, the cell media were removed and replaced with 100 μL aliquots of fresh medium containing MeONPs at concentrations of 0, 12.5, 25, 50, 100, and 200 μg/mL. The cells were incubated for 24 h at 37 °C. The supernatants were then collected for detection of LDH release and cytokine production, including TGF-β1, TNF-α, IL-1β, IL-2, IL-6, and MCP-1. The MeONPs treated cells were incubated with 120 μL of MTS working solution (5 mg/mL) in phenol red-free media for 2 h at 37 °C to examine mitochondria activity, lysed in 100 μL working solution in ATP assay kit to assess energy metabolism by luminescence, or 15 μg/mL H_2DCF-DA in the dark for 30 min at 37 °C to detect ROS generation using a microplate reader at an excitation wavelength of 488 nm and an emission wavelength of 525 nm. After incubation with colorimetric substrates in LDH, MTS, and ATP assays, the 96-well plates underwent centrifugation at 3000 rpm. Subsequently, the supernatants were transferred to new 96-well plates for detection using a microplate reader. Meanwhile, lysosomal pH was determined using the Lysosensor Yellow/Blue DND-160 assay kit (40768ES50, Yishang) according to the manufacturer's instructions. Briefly, the culture media in MeONP-treated cells was replaced with 100 μL PBS containing 1 μM DND-160 probes. After incubating at 37 °C for 3 min, the cells were washed twice with PBS and detected using a microplate reader at 384 nm excitation and 540 nm emission. The relative fold changes of indexes were calculated by the following equation:

$$FC = \frac{I_{NP} - I_{BL}}{I_{Ctrl} - I_{BL}} \quad (3)$$

where I_{NP}, Ic_{trl}, and I_{BL} represent the measured intensity of indexes in MeONP-treated cells, vehicle solution-treated cells, and blanks, respectively.

Assessment of lung fibrosis in mice

All animal experiments were approved by the Ethics Committee of Soochow University (Approval NO. 202108A0167). A total of 208 animals were used to determine chronic lung fibrosis induced by 52 different MeONPs, with four animals in each group ($n = 4$). Female C57Bl/6 mice (8 weeks old) were purchased from Nanjing Peng Sheng Biological Technology (Nanjing, China). We deliberately selected female mice for lung fibrosis tests as they are reported to be more sensitive than male ones in pulmonary nanotoxicity studies[63,64]. Animals were housed in groups of four under standard laboratory conditions (25 °C; 60% relative humidity; 12 h light, 12 h dark cycle) and hygiene status (autoclaved food and acidified water) according to Soochow University guidelines for the care and treatment of laboratory animals. Feedstuff were purchased from Shuangshi Experimental Animal Feed Corporation (Suzhou, China) (catalog number: SSFZP01-002). Animals were exposed to MeONPs by an oropharyngeal instillation method. Briefly, MeONPs were suspended in PBS at 1 mg/mL by a probe sonication (32 W) for 10 s. The animals were anesthetized by intraperitoneal injection of sodium pentobarbital (200 mg/kg) in a total volume of 100 uL. The anesthetized animals were held in a vertical position for the pulmonary aspiration of MeONP suspension (with a dose of 2 mg/kg) at the back of the tongue. Animals included in the vehicle and positive controls received 50 uL of PBS and 2 mg/kg quartz, respectively. The mice were exposed once a week for 3 weeks and sacrificed on day 90 by overdose of sodium pentobarbital

(400 mg/kg). Bronchoalveolar lavage fluids (BALFs) and lung tissues were collected according to previous studies[10]. Briefly, the trachea was cannulated, and then the lungs were gently lavaged three times with 1 mL of sterile PBS to obtain BALF. Aliquots of 50 uL BALF were used to measure TGF-β1 levels by the ELISA kits (BDLISA, China). Lung tissues were collected and stained Masson's Trichrome staining according to a standard protocol[65]. The collagen deposition levels of the 203 mice were estimated according to the method reported by ref. 66.

Construction of the MFF models

We developed classification models for lung fibrosis using eight different machine learning algorithms, namely C4.5 decision tree (DTr), random forest (RF), logistic regression (LGR), k-nearest neighbor (k-NN), locally weighted learning (LWL), support vector machine (SVM), Bayesnet, and decision table (DTa). These classifiers represented various categories of supervised classifiers such as trees, Bayes, and rules. All 52 MeONPs were randomly divided into a training set (40 MeONPs) and a test set (12 MeONPs) prior to conducting any characterization and testing. The training set produced 156 in vivo datapoints, while the test set generated 47 datapoints. To avoid information leaking, we included all four datapoints of the same MeONP in either the training or test set. The criteria for classifying datapoints of MeONPs as fibrogenic potential were $FC_{TGF\text{-}\beta1} \geq 2$ or Ashcroft score ≥2.

To optimize the model's performance, we exploited a tenfold cross-validation (multiple random state) procedure based on a grid search to determine the best parameters in the machine learning methods. We performed all procedures using Weka software (Ver 3.8.5). We applied tenfold cross-validation on the training set to assess the prediction accuracy of the models. External validation was performed on the test set. The performances of models were evaluated based on true positives (TP), true negatives (TN), false positives (FP), and false negatives (FN). Model performance was evaluated using five metrics: sensitivity (SE) = TP/(TP + FN), specificity (SP) = TN/(TN + FP), overall predictive accuracy (ACC) = (TP + TN)/(TP + FP + TN + FN), F1 score = 2 × SE × SP/(SE + SP), and Matthews' correlation coefficient (MCC) = (TP × TN − FP × FN)/√(TP + FP)(TP + FN)(TN + FP)(TN + FN). MCC ranges from −1 to +1, with extreme values of −1 and +1 in the case of perfect misclassification and perfect classification, respectively. We also calculated AUC by plotting the TP rate versus the FP rate at various threshold settings. We considered the performance of a model "excellent" if AUC ≥0.9, "very poor" if AUC <0.6, "poor" if 0.7 > AUC ≥0.6, "fair" if 0.8 > AUC ≥0.7, and "good" if 0.9 > AUC ≥0.8.

We characterized the applicability domain of the prediction model using a descriptor standardization approach[50]. Seven descriptors are combined to characterize the applicability domain of the prediction model, including IL-1β, NADH in macrophages, TGF-β1, dissolution in PSF, zeta potential, hydrodynamic size, and NADH in epithelial cells. Briefly, a datapoint was considered an outlier if all normalized descriptors for the datapoint were greater than 3; otherwise, it was a non-outlier. SHAP analysis was performed using Python (V 3.9).

Coculture of THP-1, BEAS-2B, and Wi-38/VA-13 cells

WI-38/VA-13 (catalog number: CCL-75.1) cells were obtained from ATCC. Cellular coculture was performed using the Corning Transwell-24 system with 0.4-μm pore size (Corning, NY, USA). An Oxford ring was used to divide the lower chamber into inner and outer areas. Aliquots (200 μL) of THP-1/THP-1^{KD} cell suspension (5×10^4/mL) in BEGM were seeded into the lower inner chamber inside the Oxford ring. BEAS-2B/BEAS-$2B^{KD}$ cell suspensions (5×10^4/mL, 600 μL) were seeded into the lower outer chamber. Aliquots (200 μL) of Wi-38/VA-13 cell suspensions (1×10^4/mL) were seeded into the upper chamber. After overnight incubation, the cell culture media were replaced with 1000 μL nanoparticle suspensions for further incubation. After 24 h, the cell viability in the upper chamber was assessed using the MTS assay. The newborn Wi-38/VA-13 cells were labeled with Click-iT™ EdU kit (Thermo Fisher, USA) for confocal imaging.

Statistics and reproducibility

Unless otherwise noted, at least three independent experiments were performed for abiotic and in vitro tests. Statistical significance was evaluated using a two-tailed Student's *T*-test.

Reporting summary

Further information on research design is available in the Nature Portfolio Reporting Summary linked to this article.

Data availability

The data that support the findings of this study are available from the figshare (https://doi.org/10.6084/m9.figshare.24354916). Source data are provided with this paper.

Code availability

The codes and software are available for noncommercial use at GitHub (https://github.com/huangyang2023/NILFPv1.0.0). https://doi.org/10.5281/zenodo.14043988[67].

References

1. Nanotechnology Products Database (NPD). https://product.statnano.com (2023).
2. Kokot, H. et al. Prediction of chronic inflammation for inhaled particles: the impact of material cycling and quarantining in the lung epithelium. *Adv. Mater.* **32**, 2003913 (2020).
3. Garcia-Mouton, C., Hidalgo, A., Cruz, A. & Perez-Gil, J. The lord of the lungs: the essential role of pulmonary surfactant upon inhalation of nanoparticles. *Eur. J. Pharm. Biopharm.* **144**, 230–243 (2019).
4. Liu, S. & Xia, T. Continued efforts on nanomaterial-environmental health and safety is critical to maintain sustainable growth of nanoindustry. *Small* **16**, 2000603 (2020).
5. Wu, Z. et al. Inflammation increases susceptibility of human small airway epithelial cells to pneumonic nanotoxicity. *Small* **16**, 2000963 (2020).
6. Zhang, H. et al. Use of metal oxide nanoparticle band gap to develop a predictive paradigm for oxidative stress and acute pulmonary inflammation. *ACS Nano* **6**, 4349–4368 (2012).
7. Cai, X. et al. Multi-hierarchical profiling the structure-activity relationships of engineered nanomaterials at nano-bio interfaces. *Nat. Commun.* **9**, 4416 (2018).
8. Li, R. et al. Surface interactions with compartmentalized cellular phosphates explain rare earth oxide nanoparticle hazard and provide opportunities for safer design. *ACS Nano* **8**, 1771–1783 (2014).
9. Zhu, M. et al. Cell-penetrating nanoparticles activate the inflammasome to enhance antibody production by targeting microtubule-associated protein 1-light chain 3 for degradation. *ACS Nano* **14**, 3703–3717 (2020).
10. Huang, Y. et al. Quantitative structure-activity relationship models for predicting inflammatory potential of metal oxide nanoparticles. *Environ. Health Perspect.* **128**, 67010 (2020).
11. Barosova, H. et al. Use of EpiAlveolar lung model to predict fibrotic potential of multiwalled carbon nanotubes. *ACS Nano* **14**, 3941–3956 (2020).
12. Wang, X. et al. Toxicological profiling of highly purified metallic and semiconducting single-walled carbon nanotubes in the rodent lung and *E. coli*. *ACS Nano* **10**, 6008–6019 (2016).
13. Jiang, W. et al. Pro-inflammatory and pro-fibrogenic effects of ionic and particulate arsenide and indium-containing semiconductor materials in the murine lung. *ACS Nano* **11**, 1869–1883 (2017).
14. Rahman, L. et al. 21st century tools for nanotoxicology: transcriptomic biomarker panel and precision-cut lung slice organ

mimic system for the assessment of nanomaterial-induced lung fibrosis. *Small* **16**, 2000272 (2020).
15. Zhu, M. et al. Comparative study of pulmonary responses to nano- and submicron-sized ferric oxide in rats. *Toxicology* **247**, 102–111 (2008).
16. Jiang, J. et al. Intracellular dehydrogenation catalysis leads to reductive stress and immunosuppression. *Nat. Nanotechnol.* https://doi.org/10.1038/s41565-025-01870-y. (2025).
17. Schraufnagel, D. E. The health effects of ultrafine particles. *Exp. Mol. Med.* **52**, 311–317 (2020).
18. Oberdorster, C. et al. Principles for characterizing the potential human health effects from exposure to nanomaterials: elements of a screening strategy. *Part. Fibre Toxicol.* **2**, 8 (2005).
19. Anonymous. The risks of nanomaterial risk assessment. *Nat. Nanotechnol.* **15**, 163–163 (2020).
20. Choi, J. Y., Ramachandran, G. & Kandlikar, M. The impact of toxicity testing costs on nanomaterial regulation. *Environ. Sci. Technol.* **43**, 3030–3034 (2009).
21. Yu, F. Wei, C. Deng, P., Peng, T. & Hu, X. Deep exploration of random forest model boosts the interpretability of machine learning studies of complicated immune responses and lung burden of nanoparticles. *Sci. Adv.* **7**, eabf4130 (2021).
22. Ji, Z. et al. Machine learning models for predicting cytotoxicity of nanomaterials. *Chem. Res. Toxicol.* **35**, 125–139 (2022).
23. Roy, J. & Roy, K. Assessment of toxicity of metal oxide and hydroxide nanoparticles using the QSAR modeling approach. *Environ. Sci. Nano* **8**, 3395–3407 (2021).
24. Labouta, H. I., Asgarian, N., Rinker, K. & Cramb, D. T. Meta-analysis of nanoparticle cytotoxicity via data-mining the literature. *ACS Nano* **13**, 1583–1594 (2019).
25. Oh, E. et al. Meta-analysis of cellular toxicity for cadmium-containing quantum dots. *Nat. Nanotechnol.* **11**, 479 (2016).
26. Cao, J. et al. Computer-aided nanotoxicology: risk assessment of metal oxide nanoparticles via nano-QSAR. *Green. Chem.* **22**, 3512–3521 (2020).
27. Huang, Y. et al. Use of dissociation degree in lysosomes to predict metal oxide nanoparticle toxicity in immune cells: machine learning boosts nano-safety assessment. *Environ. Int.* **164**, 107258 (2022).
28. Yan, X. L., Sedykh, A., Wang, W. Y., Yan, B. & Zhu, H. Construction of a web-based nanomaterial database by big data curation and modeling friendly nanostructure annotations. *Nat. Commun.* **11**, 2519 (2020).
29. Ban, Z. et al. Machine learning predicts the functional composition of the protein corona and the cellular recognition of nanoparticles. *Proc. Natl Acad. Sci. USA* **117**, 10492–10499 (2020).
30. Friedersdorf, L. E., Bjorkland, R., Klaper, R. D., Sayes, C. M. & Wiesner, M. R. Fifteen years of nanoEHS research advances science and fosters a vibrant community. *Nat. Nanotechnol.* **14**, 996–998 (2019).
31. Wyrzykowska, E. et al. Representing and describing nanomaterials in predictive nanoinformatics. *Nat. Nanotechnol.* **17**, 924–932 (2022).
32. Tung Xuan, T. et al. Quasi-SMILES-based nano-quantitative structure-activity relationship model to predict the cytotoxicity of multiwalled carbon nanotubes to human lung cells. *Chem. Res. Toxicol.* **31**, 183–190 (2018).
33. Forest, V. et al. Towards an alternative to nano-QSAR for nanoparticle toxicity ranking in case of small datasets. *J. Nanopart. Res.* **21**, 95 (2019).
34. Gajewicz, A. et al. Towards understanding mechanisms governing cytotoxicity of metal oxides nanoparticles: Hints from nano-QSAR studies. *Nanotoxicology* **9**, 313–325 (2015).
35. Le, T. C. et al. An experimental and computational approach to the development of ZnO nanoparticles that are safe by design. *Small* **12**, 3568–3577 (2016).
36. Hansjosten, I. et al. Microscopy-based high-throughput assays enable multi-parametric analysis to assess adverse effects of nanomaterials in various cell lines. *Arch. Toxicol.* **92**, 633–649 (2018).
37. Puzyn, T. et al. Using nano-QSAR to predict the cytotoxicity of metal oxide nanoparticles. *Nat. Nanotechnol.* **6**, 175–178 (2011).
38. Mu, Y. et al. Predicting toxic potencies of metal oxide nanoparticles by means of nano-QSARs. *Nanotoxicology* **10**, 1207–1214 (2016).
39. Boyles, M. S. P. et al. Multi-walled carbon nanotube induced frustrated phagocytosis, cytotoxicity and pro-inflammatory conditions in macrophages are length dependent and greater than that of asbestos. *Toxicol. Vitr.* **29**, 1513–1528 (2015).
40. Gosens, I. et al. Organ burden and pulmonary toxicity of nano-sized copper (II) oxide particles after short-term inhalation exposure. *Nanotoxicology* **10**, 1084–1095 (2016).
41. Zhong, S. et al. Machine learning: new ideas and tools in environmental science and engineering. *Environ. Sci. Technol.* **55**, 12741–12754 (2021).
42. Guan, Y. et al. Pathological comparison of rat pulmonary models induced by silica nanoparticles and indium-tin oxide nanoparticles. *Int. J. Nanomed.* **17**, 4277–4292 (2022).
43. Chang, X. et al. Nano nickel oxide promotes epithelial-mesenchymal transition through transforming growth factor β1/smads signaling pathway in A549 cells. *Environ. Toxicol.* **35**, 1308–1317 (2020).
44. Zhang, Y. B., Mo, Y. Q., Zhang, Y., Yuan, J. L. & Zhang, Q. W. MMP-3-mediated cleavage of OPN is involved in copper oxide nanoparticle-induced activation of fibroblasts. *Part. Fibre Toxicol.* **20**, 22 (2023).
45. Cho, W.-S. et al. Metal oxide nanoparticles induce unique inflammatory footprints in the lung: important implications for nanoparticle testing. *Environ. Health Perspect.* **118**, 1699–1706 (2010).
46. Presume, M. et al. Exposure to metal oxide nanoparticles administered at occupationally relevant doses induces pulmonary effects in mice. *Nanotoxicology* **10**, 1535–1544 (2016).
47. Henderson, N. C., Rieder, F. & Wynn, T. A. Fibrosis: from mechanisms to medicines. *Nature* **587**, 555–566 (2020).
48. OECD. OECD guidelines for the testing of chemicals 90 day (subchronic) inhalation toxicity study. *Organisation for Economic Co-operation and Development (OECD)* (2018).
49. Stone, V. et al. A framework for grouping and read-across of nanomaterials- supporting innovation and risk assessment. *Nano Today* **35**, 100941 (2020).
50. Roy, K., Kar, S. & Ambure, P. On a simple approach for determining applicability domain of QSAR models. *Chemometr. Intell. Lab. Syst.* **145**, 22–29 (2015).
51. Cai, X. M. et al. Molecular mechanisms, characterization methods, and utilities of nanoparticle biotransformation in nanosafety assessments. *Small* **16**, 19 (2020).
52. Chetwynd, A. J. & Lynch, I. The rise of the nanomaterial metabolite corona, and emergence of the complete corona. *Environ. Sci. Nano* **7**, 1041–1060 (2020).
53. Wheeler, K. E. et al. Environmental dimensions of the protein corona. *Nat. Nanotechnol.* **16**, 617–629 (2021).
54. Liao, C.-M., Chiang, Y.-H. & Chio, C.-P. Assessing the airborne titanium dioxide nanoparticle-related exposure hazard at workplace. *J. Hazard. Mater.* **162**, 57–65 (2009).
55. Xing, M. et al. Workplace exposure to airborne alumina nanoparticles associated with separation and packaging processes in a pilot factory. *Environ. Sci. Process. Impacts* **17**, 656–666 (2015).
56. Xing, M. et al. Exposure characteristics of ferric oxide nanoparticles released during activities for manufacturing ferric oxide nanomaterials. *Inhal. Toxicol.* **27**, 138–148 (2015).
57. Xu, S. et al. Vacancies on 2D transition metal dichalcogenides elicit ferroptotic cell death. *Nat. Commun.* **11**, 3484 (2020).
58. Wang, Z. Y., Chen, J. W. & Hong, H. X. Developing QSAR models with defined applicability domains on PPARγ binding affinity using large data sets and machine learning algorithms. *Environ. Sci. Technol.* **55**, 6857–6866 (2021).

59. Casey, W. M. et al. Evaluation and optimization of pharmacokinetic models for in vitro to in vivo extrapolation of estrogenic activity for environmental chemicals. *Environ. Health Perspect.* **126**, 097001 (2018).
60. Wang, H., Wang, Z., Chen, J. & Liu, W. Graph attention network model with defined applicability domains for screening PBT chemicals. *Environ. Sci. Technol.* **56**, 6774–6785 (2022).
61. Booth, A. & Jensen, K. A. NANoREG D4.12 SOP probe sonicator calibration for ecotoxicological testing. https://www.rivm.nl/en/documenten/nanoreg-d412-sop-probe-sonicator-calibration-for-ecotoxicological-testing (2018).
62. Gao, M. et al. Two-dimensional tin selenide (SnSe) nanosheets capable of mimicking key dehydrogenases in cellular metabolism. *Angew. Chem. Int. Ed.* **59**, 3618–3623 (2020).
63. Zhang, X. et al. Sex-dependent depression-like behavior induced by respiratory administration of aluminum oxide nanoparticles. *Int. J. Environ. Res. Public Health* **12**, 15692–15705 (2015).
64. Ray, J. L. & Holian, A. Sex differences in the inflammatory immune response to multi-walled carbon nanotubes and crystalline silica. *Inhal. Toxicol.* **31**, 285–297 (2019).
65. Foot, N. C. The Masson trichrome staining methods in routine laboratory use. *Stain Technol.* **8**, 101–110 (1933).
66. Ashcroft, T., Simpson, J. M. & Timbrell, V. Simple method of estimating severity of pulmonary fibrosis on a numerical scale. *J. Clin. Pathol.* **41**, 467–470 (1988).
67. Huang, Y. et al. Multimodal Feature Fusion Machine Learning for Predicting Chronic Injury Induced by Engineered Nanomaterials, Github repository. https://doi.org/10.5281/zenodo.14043988 (2025).

Acknowledgements

This work was supported by the National Key Research and Development Program (2022YFC3902104 (X. Li), 2022YFE0124000 (X.C.)) of China, National Natural Science Foundation (22176023 (X. Li), 22406080 (Y.H.)) of China, the Fundamental Research Funds for the Central Universities (DUT22QN216 (X. Li)), the financial support of the European Union under the REFRESH-Research Excellence For Region Sustainability and High-tech Industries project (CZ.10.03.01/00/22003/0000048 (R.L.)) via the Operational Program Just Transition, and the Natural Science Foundation (ZR2024QB094 (Y. Huang)) of Shandong Province. We thank T. A. Patterson from the National Center for Toxicological Research, US Food and Drug Administration, for his contribution to the improvement of the manuscript. This article reflects the views of the authors and does not necessarily reflect those of the US Food and Drug Administration.

Author contributions

X. Li, X.C., and R.L. conceived the idea and designed the experiments. Y.H. established the predictive model. J.C. performed most of the cell and animal experiments. Q.X. performed an ELISA assay. Q.Y. contributed to the histology assay of animal lungs. X. Liu performed the characterization of MeONPs. The writing of the manuscript was led by R.L., X. Li, and X.C. with participation from J.C. and H.H.

Competing interests

The authors declare no competing interests.

Additional information

Supplementary information The online version contains supplementary material available at https://doi.org/10.1038/s41467-025-58016-w.

Correspondence and requests for materials should be addressed to Xuehua Li, Xiaoming Cai or Ruibin Li.

Peer review information *Nature Communications* thanks Iseult Lynch, Hao Zhu and the other, anonymous, reviewer(s) for their contribution to the peer review of this work. A peer review file is available.